

**Electron Shuttle in MOF Derived TiO₂/CuO Heterojunction
Boosts Light Driven Hydrogen Evolution**

Journal:	<i>Journal of Materials Chemistry A</i>
Manuscript ID	TA-ART-12-2020-012220.R1
Article Type:	Paper
Date Submitted by the Author:	19-Jan-2021
Complete List of Authors:	Zhang, Yunbo; Marquette University, Chemistry Hu, Wenhui; Marquette University, Chemistry Wang, Denan; Marquette University, Department of Chemistry Reinhart, Benjamin; Argonne National Laboratory, Huang, Jier; Marquette University, Chemistry

ARTICLE

Electron Shuttle in MOF Derived TiO₂/CuO Heterojunction Boosts Light Driven Hydrogen Evolution

Yunbo Zhang,^{a,b†} Wenhui Hu,^{b†} Denan Wang,^b Benjamin J. Reinhart,^c and Jier Huang^{*b}

Received 00th January 20xx,
Accepted 00th January 20xx

DOI: 10.1039/x0xx00000x

Metal organic frameworks (MOFs) have emerged as a novel template to develop porous photocatalytic materials for solar fuel conversion. In this work, we report the synthesis, charge separation dynamics, and photocatalytic performance of TiO₂/CuO heterostructure derived from mixed-phase MOFs based on Ti and Cu metal nodes, which demonstrates significantly enhanced catalytic activity for hydrogen evolution reaction (HER) than metal oxides derived from single node MOF. More importantly, using transient absorption spectroscopy, we identified the specific role each component in heterostructure plays and unravel the key intermediate species that is responsible for the exceptional photocatalytic activity of the heterostructure. We found that HER initiates with ultrafast electron transfer (< 150 fs) from the molecular photosensitizer to the conduction band of TiO₂, where TiO₂ acts as an electron mediator and shuttles the electron to CuO cocatalyst, facilitating charge separation and ultimately boosting HER efficiency. These results not only demonstrate the great potential of using mixed-phase MOFs as template to synthesize mesoporous heterostructure photocatalysts but also provide important insight on the HER mechanism.

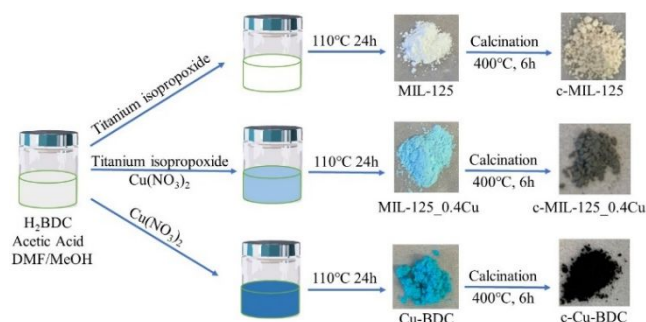
Introduction

Metal organic frameworks (MOFs) are a novel class of porous materials constructed by metal ions or clusters interconnected by multidentate organic connectors.¹⁻¹¹ Due to their unique properties such as large surface area, high porosity, and structural diversity, they have demonstrated great potentials in a wide array of applications including gas storage and separation,¹² sensing,^{13, 14} catalysis,¹⁵⁻¹⁸ and drug delivery.^{19, 20} Moreover, due to their capability to maintain porous structure after thermal and/or chemical treatment, recent efforts in the field have extended the use of MOFs as templates for preparing porous semiconductor photocatalysts.²¹⁻²³ For example, via thermal treatment or sulfidation process of MOFs, porous materials such as metal oxides,²⁴ carbon materials,²⁵⁻²⁷ and metal sulfides²⁸ have been developed and demonstrated enhanced photocatalytic performance than those prepared using traditional solid state methods. This is primarily attributed to that the MOF-derived materials inherit large surface area and uniform pore structure from MOFs, which facilitates maximizing the density of active sites and provides easy access of reaction substrates. In addition, facile synthesis of MOF-derived porous heterostructure based on the combination of semiconductor/semiconductor or semiconductor/metal have

also been reported and demonstrated efficient photocatalytic performance for various photocatalytic reactions.²⁹⁻³² This can be attributed to the structural versatility of MOFs as the building blocks of MOFs can be readily tuned to include the desired (mixed)metals/elements for heterojunction.

Among the large number of MOF-derived heterostructure materials that have been developed for photocatalytic applications, TiO₂ based heterostructure (e.g. TiO₂/Fe₂O₃/Pt, TiO₂/MoS₂, TiO₂/Co₃O₄) are one of the most promising materials for photocatalytic hydrogen evolution reaction (HER) owing to their high catalytic activity, low cost, and nontoxicity.³³⁻³⁵ However, majority of them were fabricated by calcination of MOF composites that combine a pre-existing semiconductor with MOF, leading to the difficulty in controlling the distribution and poor interaction of TiO₂ with cocatalysts/photosensitizer. In response to this challenge, in this work, we report the synthesis of TiO₂/CuO mesoporous heterostructure by calcinating a mixed phase MOF by incorporating Cu node into Ti based MOF (Cu doped MIL-125),^{23, 36} where the atomic ratio of Ti and Cu in the heterostructure can be readily tuned by feeding the different

Scheme 1. The synthetic scheme for c-MIL-125, c-MIL-125_0.4Cu, and c-Cu-BDC.



^a School of Applied Physics and Materials, Wuyi University, Jiangmen, 529020, China

^b Department of Chemistry, Marquette University, Milwaukee, Wisconsin, 53201

^c X-ray Science Division, Argonne National Laboratory, Argonne, Illinois, 60349

*Corresponding Author: Jier Huang (jier.huang@marquette.edu)

Electronic Supplementary Information (ESI) available: FTIR, EXAFS, XAS fitting results, N₂ adsorption/desorption isotherm, HER conditions, EDX, UV-visible absorption and XRD before and after catalysis. See DOI: 10.1039/x0xx00000x

concentrations of the starting metal salts. We show that, in the presence of molecular photosensitizer ($[\text{Ru}(\text{bpy})_3]^{2+}$, bpy = 2,2'-bipyridine), TiO_2/CuO mesoporous heterostructure can efficiently catalyse HER with exceptional catalytic performance (106,419 $\mu\text{mol H}_2/\text{g}$ heterostructure) and long durability (> 22 hours). More interestingly, using transient absorption spectroscopy, we found that the significantly enhanced photocatalytic activity in TiO_2/CuO mesoporous heterostructure can be attributed to the ultrafast electron transfer from $[\text{Ru}(\text{bpy})_3]^{2+}$ to TiO_2 (< 150 fs), where TiO_2 acts as an electron mediator and effectively shuttles electron to CuO cocatalyst, facilitating charge separation and ultimately boosting photocatalytic performance.

Experimental

Materials and Reagents

Titanium(IV) isopropoxide ($\geq 97\%$, Aldrich), Copper(II) nitrate hydrate (98%, ACS reagent, Sigma-Aldrich), Terephthalic acid (H_2BDC , 98%, Aldrich), N,N-Dimethylformamide (DMF, Certified ACS, Fisher Chemical), Methanol (Certified ACS, Fisher Chemical), Acetonitrile (HPLC Grade, 99.99%, Fisher Chemical), Triethanolamine (TEOA, reagent grade, 98%, Sigma-Aldrich), and Acetic acid (Certified ACS, Fisher Chemical), are used directly without further purification. $[\text{Ru}(\text{bpy})_3]^{2+}$ (bpy = 2,2'-bipyridine) was synthesized according to the published literature procedure.³⁷

The synthesis of MIL-125, Cu-BDC, and MIL-125_xCu MOFs

The synthesis of single node MOFs, i.e. MIL-125 and Cu-BDC, which involves the coordination of terephthalic acid (H_2BDC) to Ti and Cu, respectively (Scheme 1), follows the method reported previously.^{36, 38, 39} In a typical synthetic procedure for MIL-125, 0.193 g of H_2BDC is dissolved in solution containing 2.17 mL of DMF and 2.17 mL of methanol. 0.455 mL of acetic acid is then added to the solution, which is followed by the addition of titanium isopropoxide (0.074 mL). The mixture is then sonicated for 10 mins at room temperature. After that, the mixture is transferred to a 20 mL scintillation vial and kept at 110 °C for 24 h. The solid formed in the mixture (MIL-125) is collected by centrifugation, which is then washed twice by DMF and methanol, respectively. The obtained MIL-125 MOFs are dried in a fume hood at room temperature for 3 hours before use. The synthesis of Cu-BDC follows the same method as that of MIL-125 except for that titanium isopropoxide is replaced by copper nitrate hydrate.

The synthesis of mixed phase Cu/Ti MOFs follows the same procedure as that of MIL-125 and Cu-BDC except for that the mixture of copper nitrate hydrate and titanium isopropoxide is used as metal precursors (Scheme 1).²³ The ratio of Cu to Ti is controlled by feeding different molar ratio of Cu to Ti in the metal precursors, i. e. 0.1:1, 0.2:1, 0.3:1, 0.4:1, 0.7:1, respectively. The obtained mixed-phase samples are denoted according to the molar ratio of Cu to Ti as MIL-125_xCu ($x=0.1, 0.2, 0.3, 0.4, \text{ and } 0.7$), where x corresponds to the molar ratio of Cu to Ti.

The synthesis of calcinated products from MIL-125, Cu-BDC, and MIL-125_xCu MOFs

To synthesize MOF-derived metal oxides, MIL-125, Cu-BDC, and MIL-125_xCu are calcined at 400°C for 6 hours, which result into the formation of mesoporous TiO_2 , CuO, and TiO_2/CuO heterostructure and are named as c-MIL-125, c-Cu-BDC, and c-MIL-125_xCu, respectively, to distinguish them from the metal oxides synthesized through conventional no-template methods. CuO prepared through conventional method without MOF template is synthesized through heating copper nitrate hydrate at 400°C for 2h⁴⁰ and used as control sample.

Photocatalytic Hydrogen Evolution Reaction (HER)

The HER is performed in a glass vial reactor with a volume of 11 mL and can be sealed with a rubber stopper under the illumination of 450 nm LED lamp.⁴¹ The general photocatalytic system includes $[\text{Ru}(\text{bpy})_3]\text{Cl}_2 \cdot 6\text{H}_2\text{O}$ (2 mg), metal oxide catalysts (0.2 mg), acetonitrile (3.8 mL), and TEOA (0.2 mL). The reaction mixture is purged with nitrogen for 10 mins to remove oxygen before the photocatalytic reaction. 200 μL of the headspace gas is injected into the gas chromatography for quantitative measurements.

Standard Characterization

UV-Visible absorption and diffuse reflectance spectra are collected from a Cary 5000 UV-VIS-NIR spectrophotometer with internal diffuse reflectance accessory. The powder X-ray diffraction (XRD) patterns are collected using a Rigaku Miniflex II XRD diffractometer with Cu K α radiation. Fourier transformed infrared (FTIR) absorption spectra are measured from the solid powders by using a Thermo Fisher Scientific Nicolet iS5 FTIR spectrometer with an iD3 ATR accessory. Scanning electron microscopy is performed with a JEOL JSM-6510LV operating in the secondary electron mode. Gas adsorption isotherms are performed by using the surface area analyser ASAP-2020. N_2 gas adsorption isotherm is measured at 77K using a liquid N_2 bath. The amount of H_2 generated is quantified using Agilent 490 micro gas chromatograph (5 Å molecular sieve column).

Steady state X-ray absorption spectroscopy (XAS)

XAS spectra are measured at the beamline 12-BM-B (Ti k-edge) and 11-ID-D (Cu k-edge) at the Advanced Photon Source, Argonne National Laboratory. The XAS data at Ti k-edge are collected under room temperature with fluorescence mode using a 13-element germanium solid-state detector. The Ti metal foil is used for energy calibration. The powder samples are dispersed on Kapton tape during the measurement. The Ti metal foil is used for energy calibration. The XAS data at Cu k-edge are collected under room temperature with absorption mode. The Cu sample pellets are prepared by mixing with boron nitride followed by pressing. The prepared pellets are covered with Kapton tape then place onto the sample holder. Cu metal foil is used for the energy calibration.

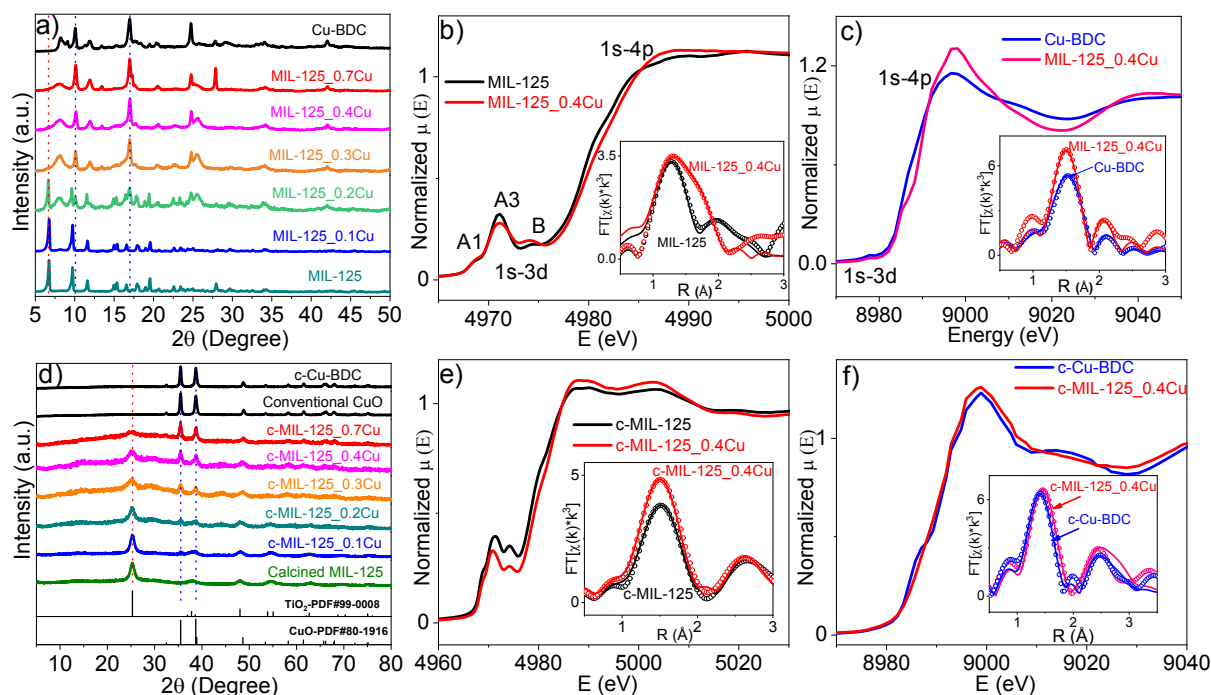


Figure 1. (a) Powder XRD patterns of MIL-125, Cu-BDC, and MIL-125_xCu ($x=0.1-0.7$); XANES spectra and EXAFS spectra in R-space with fitting (inset) of MIL-125 and MIL-125_{0.4}Cu at Ti k-edge (b) and Cu k-edge (c). (d) Powder XRD patterns of c-MIL-125, c-Cu-BDC, and c-MIL-125_xCu ($x=0.1-0.7$), as well as conventional CuO and standard PDF cards of TiO₂ and CuO; XANES spectra and EXAFS spectra in R-space with fitting (inset) of c-MIL-125 and c-MIL-125_{0.4}Cu at Ti k-edge (e) and Cu k-edge (f).

Femtosecond Transient absorption (TA) spectroscopy

The femtosecond TA spectroscopy is based on a regenerative amplified Ti-Sapphire laser system (Solstice, 800nm, < 100 fs FWHM, 3.5 mJ/pulse, 1 KHz repetition rate). The 450 nm pump, chopped at 500Hz, is generated in TOPAS from 75% of the split output from the Ti-Sapphire laser. The other 25% is used to generate broad visible probe pulses by white light generation in a Sapphire window (430-750 nm). Helios ultrafast spectrometer (Ultrafast Systems LLC) is used to collect the TA spectra. To prepare thin film for TA measurements, the MOF-derived samples (~0.8 mg) are dispersed in methanol (~1 mL), which is followed by sonication for 1h. ~5 drops of the suspension are dropped to glass surface and dried in air for 30 mins, which results in the formation of semi-transparent thin films. A few drops of [Ru(bpy)₃]²⁺ (~20 mg) in methanol (10 mL) solution are then dropped onto the surface of these films to make [Ru(bpy)₃]²⁺ sensitized metal oxide films. During the TA measurement, thin film samples are mounted on a sample stage which is continuously translated to avoid heating and permanent degradation of the sample.

Results and discussion

Synthesis and Characterization

The single node Ti-MOF (MIL-125) and single node Cu-MOF (Cu-BDC) are prepared from the reaction of terephthalic acid (H₂BDC) with titanium isopropoxide and copper nitrate hydrate, respectively (details in experimental session and Scheme 1).^{23, 36, 38, 39} The mixed-phase Cu/Ti-MOFs are synthesized following

the

same procedure as the single node MOF except that the mixture of titanium isopropoxide and copper nitrate hydrate is used. By varying the concentration of copper nitrate hydrate, mixed-phase Cu/Ti-MOFs with different atomic ratio of Cu to Ti are synthesized and denoted as MIL-125_xCu ($x=0.1-0.7$), where x represents the atomic ratio of Cu to Ti in the feeding metal precursors. The powder X-ray diffraction (XRD) patterns (Figure 1a) and FTIR spectra (Figure S1) of MIL-125 and Cu-BDC are consistent with those reported in the literature,^{23, 42} suggesting the formation of these single-node MOFs. In addition, the XRD patterns of MIL-125_xCu show features from both MIL-125 and Cu-BDC, suggesting the formation of the mixed-phase MOFs from the combination of MIL-125 and Cu-BDC. The XRD patterns of MIL-125_xCu gradually change from MIL-125 to Cu-BDC with the increasing content of Cu, which supports that Cu-BDC like phase increases with increasing Cu.

In addition to the bulk structure, the local coordination geometry at Ti and Cu center in the single-node and mixed-phase MOFs is examined using X-ray absorption spectroscopy (XAS), which is performed at Advanced Photon Source, Argonne National Laboratory. Figure 1b shows the X-ray absorption near edge structure (XANES) spectrum at Ti k-edge for MIL-125, which is mainly featured by two absorption peaks at 4968-4975 eV and 4986 eV, corresponding to 1s-3d and 1s-4p transitions, respectively. The presence of triple peaks at pre-edge region, which are labelled by A1, A3, and B according to the recent conventions^{43, 44} and have been observed previously in other Ti based materials,⁴⁵⁻⁴⁷ can be attributed to the presence of distorted TiO₆ octahedron. The quantitative analysis of the extended X-ray absorption fine structure (EXAFS) spectrum

(Figure 1b and S2, Table S1) reveals that each Ti is coordinated with three types of O atoms with Ti-O distance in the region of 1.82 Å and 2.07 Å. These results, consistent with the reported MIL-125 crystal structure,⁴⁸ further supports the formation of MIL-125. Upon the incorporation of Cu node, the XANES spectrum of MIL-125_0.4Cu at Ti k-edge also shows characteristic triple band pre-edge structure as that of MIL-125, suggesting that the local coordination geometry at Ti in MIL-125_0.4Cu retains the distorted TiO₆ octahedron. However, slight difference is observed in the XANES spectra of these two samples, where the intensity of B increases while the intensity of A3 decreases in MIL-125_0.4Cu with respect to that of MIL-125. It has been shown previously that the intensity of B and the ratio of A2/A3 reflect the degree of distortion.⁴⁴ As a result, the enhanced B and reduced A3 may result from the increasing distortion at Ti center due to Cu incorporation in MIL-125_0.4Cu. Additional difference is observed in the EXAFS spectra in R-space (inset of Figure 1b), where the first shell peak corresponding to Ti-O bond in the spectrum of MIL-125_0.4Cu extends to longer bond distance compared to that in MIL-125. This is consistent with the fitting results, where the Ti-O path with longer distance contributes more in MIL-125_0.4Cu than in MIL-125 (Table S1). These results together suggest that the introduction of Cu in MIL-125 causes the distortion of Ti local structure, which also suggests that the mixed-phase MIL-125_0.4Cu includes direct incorporation of Cu into the framework of MIL-125 rather than being in a separate framework.

In addition to Ti edge, the Cu k-edge XAS spectra are also collected and compared between MIL-125_0.4Cu and Cu-BDC. As shown in Figure 1c, the XANES spectrum of Cu-BDC at Cu k-edge is featured by a sharp absorption peak at 8896 eV corresponding to Cu 1s to 4p transition and a noticeable pre-edge feature at 8977 eV corresponding to quadrupole 1s-3d transition. Because Cu has electronic configuration of 3d¹⁰4s¹, the quadrupole 1s-3d transition is only allowed when Cu²⁺ (3d⁹) exists,^{49, 50} suggesting that Cu-BDC is dominated by Cu²⁺. The quantitative analysis on EXAFS spectrum of Cu-BDC (inset of Figure 1c) yields that each Cu is coordinated with five O atoms with two different Cu-O distances at 1.96 Å and 2.2 Å, which is consistent with the crystal structure of Cu-BDC⁵¹ and further supports the formation of Cu-BDC. Upon the introduction of Cu into MIL-125, the XANES spectrum of MIL-125_0.4Cu at Cu center (Figure 1c) shows similar pre-edge feature but slightly different white line with respect to that of Cu-BDC, suggesting that Cu²⁺ retains but the local coordination environment has somewhat changed. This is also reflected from its EXAFS spectrum (inset of Figure 1c and S2), where the intensity of Cu-O path increases compared to that in Cu-BDC. Further quantitative analysis on the EXAFS spectra (inset of Figure 1c and S2, Table S2) reveals the increase of coordination number and decrease of disorder (smaller Debye-Waller factor). These results, similar to the previous literature data,⁵² suggest that Cu replaces some of the Ti sites in MIL-125_0.4Cu, consistent with the XAS results at Ti edge.

These MOF samples are calcinated at 400°C in air for 6 hours, which result into the formation of their corresponding

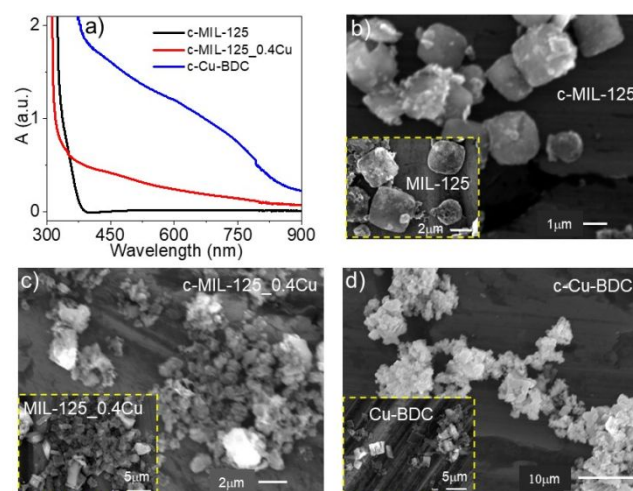


Figure 2. (a) Diffuse reflectance spectra of c-MIL-125, c-Cu-BDC, and c-MIL-125_0.4Cu; SEM images of c-MIL-125 (d), c-MIL-125_0.4Cu (e), c-Cu-BDC (f) as well as their corresponding MOFs before calcination in the insets.

semiconductor oxide or heterostructure. As shown in Figure 1d, the calcinated MIL-125 (denoted c-MIL-125) and Cu-BDC (denoted c-Cu-BDC) exhibit XRD patterns that match well with the standard PDF cards of TiO₂ and CuO, respectively, suggesting the formation of pure TiO₂ and CuO after calcination.⁵³ The XRD patterns of the products obtained after calcinating MIL-125_xCu MOFs (denoted c-MIL-125_xCu) show characteristic peaks from both TiO₂ and CuO, and gradually change from TiO₂-like to CuO-like patterns with increasing Cu content, suggesting the formation of TiO₂/CuO heterostructure with increasing amount of CuO, consistent with their corresponding MOFs. The formation of the semiconductor oxide and heterostructure is further confirmed by XAS. After calcination, the XANES spectrum of c-MIL-125_0.4Cu shows similar features as that of c-MIL-125 at Ti k-edge (Figure 1e), which are consistent with that of previous reported TiO₂ and CuO,^{45-47, 52, 54} suggesting the formation of TiO₂ in the heterostructure after calcination. At Cu edge, the XANES spectrum of c-MIL-125_0.4Cu shows almost the same features as that of c-Cu-BDC (Figure 1f), which is similar to the reported calcinated Cu-MIL-125 XANES features,⁵² confirming the conversion of Cu-BDC to CuO after calcination. However, there is slight difference in the coordination number at both Ti and Cu center in c-MIL-125_0.4Cu compared to that of c-MIL-125 and c-Cu-BDC (Table S3 and S4), respectively, suggesting that the presence of Cu/Ti metal has impact on the coordination environment of Ti/Cu in the heterostructure derived from the mixed phase MOF.

The formation of TiO₂/CuO heterostructure was further supported by diffuse reflectance (DR) spectra (Figure 2a and Figure S4), where the DR spectra of the c-MIL-125_xCu exhibit an additional absorption in visible region with respect to that of c-MIL-125 (pure TiO₂). This additional absorption band is consistent with the band observed in the c-Cu-BDC (pure CuO) and can thus be attributed to the presence of CuO in the heterostructure. The SEM images of calcinated samples show similar morphology as their derived MOFs (Figure 2b-2d), suggesting the retain of the MOF morphology. The size of the

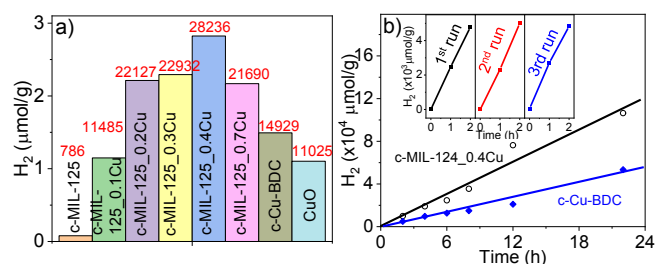


Figure 3. (a) The comparison of HER performance among c-MIL-125, c-MIL-125_xCu, and conventional CuO; (b) The HER time profile of c-MIL-125_0.4Cu and c-Cu-BDC.

calcinated samples is smaller than those MOFs, which is likely due to the removal of the organic ligands during calcination process.²³ The retain of MOF porosity is further supported by the N₂ adsorption/desorption experiment, where the calcinated heterostructure shows similar pore size as its corresponding MOF (Figure S5 and Table S5) although smaller BET surface. In addition, the EDX mapping suggests that both Cu and Ti have relatively uniform distribution in c-MIL-125_0.4Cu (Figure S6 and S7).

Photocatalytic Performance for HER

The photocatalytic performance of c-MIL-125_xCu heterostructure for hydrogen evolution reaction (HER) was examined upon the illumination by a 450 nm LED lamp in the presence of [Ru(bpy)₃]²⁺ as photosensitizer and TEOA as electron sacrificial agent in acetonitrile solution.^{41, 55} As shown in Table S6, the control experiments by omitting TEOA and [Ru(bpy)₃]²⁺ results in minimal amount of H₂, suggesting that both of them are essential for HER. On the other hand, the system without including c-MIL-125_xCu can generate 291 μmol H₂ per gram of [Ru(bpy)₃]²⁺, which has been observed previously^{41, 56} and can be attributed to that [Ru(bpy)₃]²⁺ have intrinsic photocatalytic activity for HER. In addition, the experimental conditions such as the concentration of TEOA, the concentration of the catalyst, as well as the power of LED light, are systematically varied to optimize the HER efficiency (Table S6), from which we found that the system shows best performance (19036 μmol H₂/g catalyst) when 0.2 mL TEOA, 0.2 A LED power, and 0.2 mg of c-MIL-125_0.4Cu were used. As a result, these conditions are employed for further optimizing the catalytic performance of the c-MIL-125_xCu with different content of Cu. As shown in Figure 3a, the catalytic performance increases initially with increasing Cu content (x=0.1-0.3) and reaches maximum when Cu content is 0.4. After that, the further increase of Cu content results into the decrease of HER performance. The best performance for HER found is in c-MIL-125_0.4Cu. As shown in the time profile of c-MIL-125_0.4Cu for HER (Figure 3b), c-MIL-125_0.4Cu can steadily generate H₂ for at least 22 hours, which reaches 106,419 μmol/g. This is ~36 times better than c-MIL-125 and ~2 times better than that of c-Cu-BDC, suggesting that heterostructure plays an important role in enhancing the photocatalytic activity for HER.

The cease of HER can be attributed to the degradation of [Ru(bpy)₃]²⁺, as the UV-visible absorption spectrum of [Ru(bpy)₃]²⁺ before and after catalyst has changed significantly

while the XRD patterns of c-MIL-125_0.4Cu has negligible change (Figure S8). The stability of the c-MIL-125_0.4Cu photocatalytic system was further investigated via recycling experiments, where c-MIL-125_0.4Cu was centrifuged from the catalysis mixture, washed with acetonitrile, and re-dispersed in a fresh catalysis mixture after every 2 hours of photocatalysis. As shown in the inset of Figure 3b, the catalytic activity retains for at least 3 cycles of experiment, suggesting the recyclability of the system.

Photoinduced Charge Separation Dynamics

To gain insight on the catalytic mechanism and the specific roles each component plays, we examined the charge separation dynamics of these samples using transient absorption (TA) spectroscopy. The TA spectra of the control sample, i.e. [Ru(bpy)₃]²⁺ on Al₂O₃, are first examined. Due to the significantly large band gap and high conduction band edge of Al₂O₃, neither charge transfer nor energy transfer should occur from [Ru(bpy)₃]²⁺ to Al₂O₃.⁵⁷ As shown in Figure 4a, the TA spectra of [Ru(bpy)₃]²⁺/Al₂O₃ show a negative feature < 500 nm and a broad absorption from 525-750 nm, which can be attributed to the ground state bleach (GSB) and excited state absorption (ESA) of [Ru(bpy)₃]²⁺, respectively.⁵⁸ The GSB recovers and the ESA decays simultaneously with an isosbestic point at 522 nm, suggesting that they correspond to the same relaxation process, i.e. the excited state of [Ru(bpy)₃]²⁺ returns to ground state. Compared to the TA spectra of [Ru(bpy)₃]²⁺/Al₂O₃, the TA spectra of [Ru(bpy)₃]²⁺ on c-MIL-125 (pure TiO₂) show distinct spectra features (Figure 4b), where the ESA observed in [Ru(bpy)₃]²⁺/Al₂O₃ disappears, the GSB becomes broader, and a positive absorption at > 670 nm is observed. The positive feature agrees well with the absorption of [Ru(bpy)₃]²⁺ in its oxidized state and/or electron absorption in the conduction band of TiO₂,^{58, 59} suggesting that ultrafast electron transfer (ET) occurs from [Ru(bpy)₃]²⁺ to c-MIL-125, which results in the quenching of ESA of [Ru(bpy)₃]²⁺, the formation of oxidized [Ru(bpy)₃]²⁺ and/or injected electrons in TiO₂. The ET process is further supported by the comparison of the GSB kinetic traces between [Ru(bpy)₃]²⁺/c-MIL-125 and [Ru(bpy)₃]²⁺/Al₂O₃, where the former shows a longer lived GSB (Figure 4c), which can be attributed to the slower charge recombination in the former since the charge recombination has to occur between the oxidized [Ru(bpy)₃]²⁺ and the electrons in the conduction band of c-MIL-125. Since the decay of ESA of [Ru(bpy)₃]²⁺ as well as the formation of oxidized [Ru(bpy)₃]²⁺ or electrons in TiO₂ occur immediately after the photoexcitation, we believe that the ET process is ultrafast and beyond our TA temporal resolution (~150 fs).

The TA spectra of [Ru(bpy)₃]²⁺ on c-Cu-BDC (pure CuO) was also examined under the same conditions as [Ru(bpy)₃]²⁺/c-MIL-125. Note that the TA spectra of [Ru(bpy)₃]²⁺/c-Cu-BDC (Figure 4d) are dominated by the features from c-Cu-BDC (Figure 4e) with negligible spectral contribution from [Ru(bpy)₃]²⁺. This can be explained by the much larger extinction coefficient of c-Cu-BDC than that of [Ru(bpy)₃]²⁺ at the excitation wavelength (450 nm), resulting into that majority photons are absorbed by c-Cu-

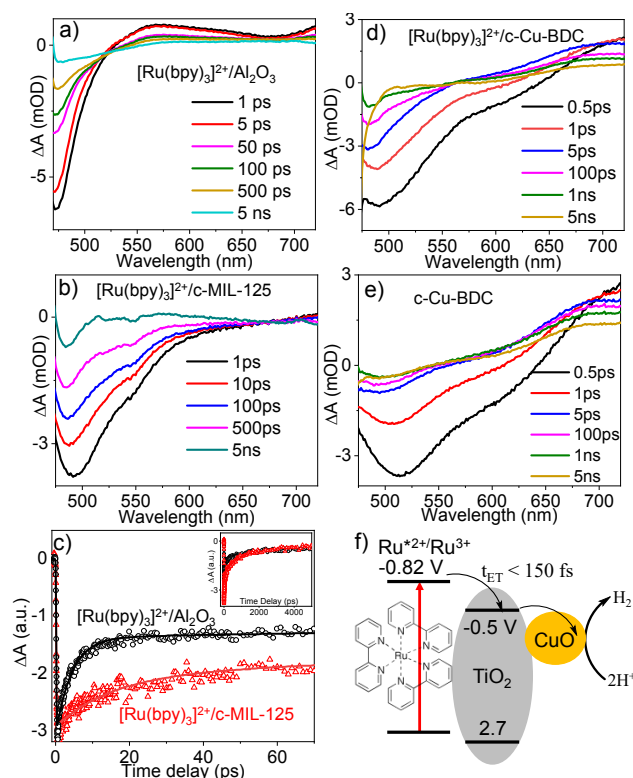


Figure 4. Transient absorption spectra of $[\text{Ru}(\text{bpy})_3]^{2+}/\text{Al}_2\text{O}_3$ (a), $[\text{Ru}(\text{bpy})_3]^{2+}/\text{c-MIL-125}$ (b), $[\text{Ru}(\text{bpy})_3]^{2+}/\text{c-Cu-BDC}$ (d), and c-Cu-BDC (e) following 450 nm excitation. (c) The comparison of kinetic traces at 500 nm between $[\text{Ru}(\text{bpy})_3]^{2+}/\text{Al}_2\text{O}_3$ and $[\text{Ru}(\text{bpy})_3]^{2+}/\text{c-MIL-125}$. The open circle and triangles are the experimental data and the solid lines are their best fits. (f) The schematic diagram of charge transfer process in $[\text{Ru}(\text{bpy})_3]^{2+}/\text{c-MIL-125}_x\text{Cu}$. The potentials are versus SCE and adopted from Ref. 58 and 59.

BDC rather than $[\text{Ru}(\text{bpy})_3]^{2+}$. This issue might be addressed by selectively exciting $[\text{Ru}(\text{bpy})_3]^{2+}$ in $[\text{Ru}(\text{bpy})_3]^{2+}/\text{c-Cu-BDC}$ sample. However, the absorption of c-Cu-BDC covers the whole spectrum where $[\text{Ru}(\text{bpy})_3]^{2+}$ absorbs (Figure 2a), leading to the challenge in examining ET dynamics in $[\text{Ru}(\text{bpy})_3]^{2+}/\text{c-Cu-BDC}$. Nevertheless, $[\text{Ru}(\text{bpy})_3]^{2+}$ in the presence of c-Cu-BDC exhibits much higher HER activity than that without c-Cu-BDC , and that c-Cu-BDC without $[\text{Ru}(\text{bpy})_3]^{2+}$ shows negligible catalytic activity, suggesting that $[\text{Ru}(\text{bpy})_3]^{2+}$ and c-Cu-BDC play roles as photosensitizer and cocatalyst, respectively. In addition, the photocatalytic activity of $\text{c-MIL-125}_x\text{Cu}$ ($x=0.2-0.7$) is higher than that of c-Cu-BDC and ultrafast ET occurs from $[\text{Ru}(\text{bpy})_3]^{2+}$ to c-MIL-125 , suggesting that c-MIL-125 must play an important role in charge separation, where c-MIL-125 acts as an electron mediator by extracting electrons from $[\text{Ru}(\text{bpy})_3]^{2+}$ and shuttling them to c-Cu-BDC (Figure 4f) to perform HER.

Conclusions

In summary, we report the synthesis, charge separation, and catalytic performance of mesoporous TiO_2/CuO heterostructure derived from the mixed-phase (Cu/Ti) MOFs for HER. We show that MOF-derived TiO_2/CuO heterostructure retains the porosity of MOFs, resulting into exceptional catalytic

performance and durability for HER, which is significantly higher than the metal oxides derived from single node MOF and synthesized by conventional method. Using transient absorption spectroscopy, we show that the significantly enhanced catalytic activity of TiO_2/CuO heterostructure can be attributed to the ultrafast electron transfer from the photosensitizer to TiO_2 , where TiO_2 acts as an electron mediator, facilitating charge separation between the photosensitizer and CuO cocatalyst. These results not only demonstrate the great promise to use mixed-phase MOF as template for synthesizing semiconductor oxide heterostructure but also provide important insight on the catalytic mechanism of the heterostructure photocatalyst for HER.

Author Contributions

[†]These authors contribute equally. Y. Z. performed the synthesis, characterization, and catalytic performance of the samples; W. H. collected and performed the XAS data analysis; D. W. assisted the TA and SEM measurements; B. J. R. assisted XAS measurements; J. H. designed the project and leads the role in writing the paper. All authors participate in writing the paper.

Conflicts of interest

There are no conflicts to declare.

Acknowledgements

This work was supported by National Science Foundation (CBET-1706971). Y. Z. acknowledges the support from Wuyi University Student Fellowship. W. H. acknowledges the John J. Eisch fellowship during the 2018-2019 academic year. Use of the Advanced Photon Source at Argonne National Laboratory was supported by the U. S. Department of Energy, Office of Science, Office of Basic Energy Sciences, under Award No. DE-AC02-06CH11357. We acknowledge Christian Fiankor and Prof. Jian Zhang at University of Nebraska-Lincoln for BET measurements.

References

1. N. L. Rosi, J. Eckert, M. Eddaoudi, D. T. Vodak, J. Kim, M. O'Keeffe and O. M. Yaghi, *Science*, 2003, **300**, 1127-1129.
2. H. C. Zhou, J. R. Long and O. M. Yaghi, *Chem. Rev.*, 2012, **112**, 673-674.
3. T. R. Cook, Y. R. Zheng and P. J. Stang, *Chem. Rev.*, 2013, **113**, 734-777.
4. C. Wang, D. M. Liu and W. B. Lin, *J. Am. Chem. Soc.*, 2013, **135**, 13222-13234.
5. S. Kitagawa, R. Kitaura and S. Noro, *Angew. Chem. Int. Edit.*, 2004, **43**, 2334-2375.
6. B. Moulton and M. J. Zaworotko, *Chem. Rev.*, 2001, **101**, 1629-1658.
7. O. K. Farha, A. M. Spokoyny, K. L. Mulfort, M. F. Hawthorne, C. A. Mirkin and J. T. Hupp, *J. Am. Chem. Soc.*, 2007, **129**, 12680-12681.
8. Y. Pan, Y. Qian, X. Zheng, S. Q. Chu, Y. Yang, C. Ding, X. Wang, S. H. Yu, H. L. Jiang, *Natl. Sci. Rev.* 2021, **8**, nwaa224.

9. D. Dong, C. Yan, J. Huang, N. Lu, P. Wu, J. Wang and Z. Zhang, *J. Mater. Chem. A*, 2019, **7**, 24180-24185.
10. J.D. Xiao and H. L. Jiang, *Acc. Chem.Res.*, 2018, **52**, 356-366.
11. R. Bibi, H. Huang, M. Kalulu, Q. Shen, L. Wei, O. Oderinde, N. Li, and J. Zhou, *ACS Sustain. Chem. Eng.*, 2018, **7**, 4868-4877.
12. D. Alezi, Y. Belmabkhout, M. Suyetin, P. M. Bhatt, Ł. J. Weseliński, V. Solovyeva, K. Adil, I. Spanopoulos, P. N. Trikalitis, A.H. Emwas and M. Eddaoudi, *J. Am. Chem. Soc.*, 2015, **137**, 13308-13318.
13. Y. Cui, R. Song, J. Yu, M. Liu, Z. Wang, C. Wu, Y. Yang, Z. Wang, B. Chen and G. Qian, *Adv. Mater.*, 2015, **27**, 1420-1425.
14. X. Zhu, H. Zheng, X. Wei, Z. Lin, L. Guo, B. Qiu and G. Chen, *Chemi. Commun.*, 2013, **49**, 1276-1278.
15. K. Shen, X. Chen, J. Chen and Y. Li, *ACS Catal.*, 2016, **6**, 5887-5903.
16. C. Wang, B. An and W. Lin, *ACS Catal.*, 2018, **9**, 130-146.
17. T. Wang, L. Gao, J. Hou, S. J. Herou, J. T. Griffiths, W. Li, J. Dong, S. Gao, M.M. Titirici, R. V. Kumar, A. K. cheetham, X. Bao, Q. Fu, and S. K. Smoukov, *Nati. Commun.*, 2019, **10**, 1-9.
18. D. Li, M. Kassymova, X. Cai, S. Q. Zhang and H. L. Jiang, *Coord. Chem. Rev.*, 2020, **412**, 213262-213277.
19. M. X. Wu and Y. W. Yang, *Adv. Mater.*, 2017, **29**, 1606134.
20. X. Gao, X. Hai, H. Baigude, W. Guan and Z. Liu, *Sci. Rep.*, 2016, **6**, 37705.
21. L. Pan, T. Muhammad, L. Ma, Z.F. Huang, S. Wang, L. Wang, J.J. Zou and X. Zhang, 2016, *Appl. Catal B-Environ.*, **189**, 181-191.
22. Y. Zheng, P. Cheng, J. Xu, J. Han, D. Wang, C. Hao, H. R. Alanagh, C. Long, X. Shi and Z. Tang, *Nanoscale*, 2019, **11**, 4911-4917.
23. Y.-T. Liao, Y.-Y. Huang, H. M. Chen, K. Komaguchi, C.-H. Hou, J. Henzie, Y. Yamauchi, Y. Ide, and K. C. W. Wu, *ACS Appl. Mater. Interfaces*, 2017, **9**, 42425-42429.
24. C. Yu, Y. Wang, J. Cui, D. Yu, X. Zhang, X. Shu, J. Zhang, Y. Zhang, R. Vajtai, P. M. Ajayan and Y. Wu, *J. Mater. Chem. A*, 2018, **6**, 8396-8404.
25. Z. Liang, C. Qu, D. Xia, R. Zou and Q. Xu, *Angew. Chem. Int. Edit.*, 2018, **57**, 9604-9633.
26. W. Chaikittisilp, K. Ariga and Y. Yamauchi, *J. Mater. Chem. A*, 2013, **1**, 14-19.
27. Q. Yang, C. C. Yang, C. C. Lin and H. L. Jiang, *Angew. Chem. Int. Edit.*, 2019, **131**(11), 3549-3553.
28. X. Y. Lin, Y. H. Li, M. Y. Qi, Z. R. Tang, H. L. Jiang and Y. J. Xu, *Nanoscale Horiz.*, 2020, **5**, 714-719.
29. Y. Lin, H. Wan, F. Chen, X. Liu, R. Ma and T. Sasaki, *Dalton Trans.*, 2018, **47**, 7694-7700.
30. C. Zhang, B. Liu, X. Cheng, Z. Guo, T. Zhuang and Z. Lv, *ACS Appl. Energy Mater.*, 2019, **3**, 852-860.
31. W. Zhao and C. Liu, *RSC Advances*, 2020, **10**(25), 14550-14555.
32. L. Lu, B. Wu, W. Shi and P. Cheng, *Inorg. Chem.Front.*, 2019, **6**, 3456-3467.
33. A. Meng, L. Zhang, B. Cheng and J. Yu, *Adv. Mater.*, 2019, **31**, 1807660.
34. Q. Guo, C. Zhou, Z. Ma and X. Yang, *Adv. Mater.*, 2019, **31**, 1901997.
35. Q. Guo, Z. Ma, C. Zhou, Z. Ren and X. Yang, *Chem. Rev.*, 2019, **119**, 11020-11041.
36. S. Rostamnia, H. Alamgholiloo, and X. Liu, *J. Colloid Interface Sci.*, 2016, **469**, 310-317.
37. D. Kim, D. R. Whang and S. Y. Park, *J. Am. Chem. Soc.*, 2016, **138**, 8698-8701.
38. W. P. Mounfield III, C. Han, S. H. Pang, U. Tumuluri, Y. Jiao, S. Bhattacharyya, M. R. Dutzer, S. Nair, Z. Wu, R. P. Lively, D. S. Sholl and K. S. Walton, *J. Phys. Chem. C*, 2016, **120**, 27230-27240.
39. G. H. Dang, Y. T. Vu, Q. A. Dong, D. T. Le, T. Truong and N. T. Phan, *Appl. Catal. A-Gen.*, 2015, **491**, 189-195.
40. T. Arai, M. Horiguchi, M. Yanagida, T. Gunji, H. Sugihara and K. Sayama, *J. Phys. Chem. C*, 2009, **113**, 6602-6609.
41. Y. Zhou, W. Hu, S. Yang, Y. Zhang, J. Nyakuchena, K. Duisenova, S. Lee, D. Fan and J. Huang, *J. Phys. Chem. C*, 2019, **124**, 1405-1412.
42. Y. Chen, Y. Du, P. Liu, J. Yang, L. Li and J. Li, *Environ. Sci. Technol.*, 2020, **54**, 3636-3642.
43. V. Luca, S. Djajanti and R. F. Howe, *J. Phys. Chem. B*, 1998, **102**, 10650-10657.
44. P. T. Hsiao, M. D. Lu, Y. L. Tung and H. S. Teng, *J. Phys. Chem. C*, 2010, **114**, 15625-15632.
45. R. Brydson, H. Sauer, W. Engel, J. M. Thomas, E. Zeitler, N. Kosugi and H. Kuroda, *J. Phys. Condens. Matter*, 1989, **1**, 797-812.
46. Z. Y. Wu, G. Ouyard, P. Gressier and C. R. Natoli, *Physical Review B*, 1997, **55**, 10382-10391.
47. K. Schneider, D. Zajac, M. Sikora, C. Kapusta, K. Michalow-Mauke, T. Graule and M. Rekas, *Radiation Physics and Chemistry*, 2015, **112**, 195-198.
48. M. Dan-Hardi, C. Serre, T. Frot, L. Rozes, G. Maurin, C. Sanchez and G. Ferey, *J. Am. Chem. Soc.*, 2009, **131**, 10857-10859.
49. J. Ludwig, L. An, B. Pattengale, Q. Y. Kong, X. Y. Zhang, P. X. Xi and J. E. Huang, *J. Phys. Chem. Lett.*, 2015, **6**, 2671-2675.
50. W. H. Hu, J. Ludwig, B. Pattengale, S. Z. Yang, C. M. Liu, X. B. Zuo, X. Y. Zhang and J. Huang, *J. Phys. Chem. C*, 2018, **122**, 974-980.
51. C. G. Carson, K. Hardcastle, J. Schwartz, X. T. Liu, C. Hoffmann, R. A. Gerhardt and R. Tannenbaum, *Eur. J. Inorg. Chem.*, 2009, 2338-2343.
52. Y. Yoshida and Y. Izumi, *J. Catal.*, 2015, **332**, 1-12.
53. D. Lu, O. A. Zelekew, A. K. Abay, Q. Huang, X. Chen and Y. Zheng, *RSC Advances*, 2019, **9**, 2018-2025.
54. P. C. Angelome, L. Andrini, M. E. Calvo, F. G. Requejo, S. A. Birmes and G. Soler-Illia, *J. Phys. Chem. C*, 2007, **111**, 10886-10893.
55. S. Yang, B. Pattengale, E. L. Kovrigin and J. Huang, *ACS Energy Lett.*, 2017, **2**, 75-80.
56. C. C. Hou, T. T. Li, S. Cao, Y. Chen and W. F. Fu, *J. Mater. Chem. A*, 2015, **3**, 10386-10394.
57. B. Pattengale, S. Z. Yang, S. Lee and J. Huang, *ACS Catal.*, 2017, **7**, 8446-8453.
58. D. Kuciauskas, J. E. Monat, R. Villahermosa, H. B. Gray, N. S. Lewis and J. K. McCusker, *J. Phys. Chem. B*, 2002, **106**, 9347-9358.
59. K. Vinodgopal, X. Hua, R. L. Dahlgren, A. G. Lappin, L. K. Patterson and P. V. Kamat, *J. Phys. Chem.*, 1995, **99**, 10883-10889.